© 2020. Published by The Company of Biologists Ltd | Development (2020) 147, dev183830. doi:10.1242/dev.183830

TECHNIQUES AND RESOURCES

RESEARCH ARTICLE

A genetic system for tissue-specific inhibition of cell proliferation

Wenjuan Pu[1,2,*], Ximeng Han[1,3,*], Lingjuan He[1,2], Yan Li[1,2], Xiuzhen Huang[1,2], Mingjun Zhang[1], Zan Lv[1], Wei Yu[1,2], Qing-Dong Wang[4], Dongqing Cai[5], Jinjin Wang[6], Ruilin Sun[6], Jian Fei[6], Yong Ji[7,8], Yu Nie[9] and Bin Zhou[1,2,3,5,7,10,‡]

ABSTRACT

Cellular proliferation is a basic process during organ development, tissue homeostasis and disease progression. Likewise, after injury typically multiple cell lineages respond to various cues and proliferate to initiate repair and/or remodeling of the injured tissue. Unravelling the specific role of proliferation of one cell type and its lineage in the context of the whole organism during tissue regeneration and/or disease progression would provide valuable information on these processes. Here, we report a new genetic system that allows cell proliferation to be inhibited in a tissue-specific manner. We generated Cre- or Dre-inducible p21-GFP (ip21-GFP) transgenic mice that enable experimentally induced permanent cell cycle arrest of specific cell lineages of interest, while genetically marking these cells. This system allows for the inhibition of pathogenic cell proliferation. We found that cardiac fibroblast proliferation inhibition significantly reduced scar formation, and promoted neovascularization and cardiomyocyte survival. Additionally, we found that inhibition of one type of cell proliferation (namely, hepatocytes) induces the lineage conversion of another type cells (i.e. ductal cells) during tissue regeneration. These results validate the use of ip21-GFP mice as a new genetic tool for cell lineage-specific inhibition of cell proliferation *in vivo*.

KEY WORDS: Cell proliferation, Genetic tools, Lineage conversion, Mouse

INTRODUCTION

During development, tissue homeostasis, disease progression, or tissue repair and regeneration after injury, cells typically proliferate to expand their numbers or compensate for their loss (Simons and Clevers, 2011; Hogan et al., 2014; Augustin and Koh, 2017; Mohamed et al., 2018). For example, in development, cellular proliferation occurs to ensure proper organ growth and function (Buckingham et al., 2005; Heallen et al., 2011; Tzahor and Poss, 2017). The preliminary coronary vascular plexus expands and sprouts to form new blood vessels in the ventricular wall during heart development (Red-Horse et al., 2010; Tian et al., 2013), and pre-existing coronary endothelial cells re-expand and contribute to neovascularization after myocardial infarction (He et al., 2017a). Likewise, during adult homeostasis stem cells residing in the crypt of the intestine differentiate into transit-amplifying cells that rapidly expand to make more enterocytes as the intestinal wall repeatedly sheds (Barker et al., 2007).

Further, in mouse liver homeostasis, Axin2$^+$ hepatocytes residing initially in the peri-central region of the liver lobule expand gradually to populate the liver, reaching the peri-portal region after 1 year of proliferation and migration. During liver injury, Sox9$^+$ hybrid hepatocytes in the peri-portal region expand further to re-populate the entire liver lobule (Font-Burgada et al., 2015). Also, during lung injury, stem cells residing in the bronchioalveolar duct junction differentiate and expand to provide bronchiolar or alveolar epithelial cells for lung repair and regeneration (Kim et al., 2005). Cardiomyocytes in the neonatal heart proliferate and heart apex resection stimulates their proliferation even further to regenerate the tissue after such injury (Porrello et al., 2011). Although in the adult heart cardiomyocyte turnover is low, these cells still exhibit detectable proliferation to slowly compensate for the exchange of ∼50% of these cells during a normal life span (Bergmann et al., 2009). Throughout the body, cell proliferation is involved in virtually every biological process that ranges from development to disease to regeneration.

Although cell proliferation is an important and fundamental process, it remains technically challenging to dissect the exact contribution of distinct expanding cell populations in the context of the entire organism in the setting of disease or tissue repair from other complex processes that occur in these settings. Many cell types are typically involved in disease pathogenesis and progression, and their individual expansion or cell type conversion can be either beneficial or detrimental to tissue recovery (Zeisberg et al., 2003; Ubil et al., 2014). For example, after myocardial infarction, coronary endothelial cells proliferate markedly in the infarct border due to tissue hypoxia (Zhou et al., 2011). The injury also stimulates cardiomyocyte proliferation in the border region, which could be beneficial to heart repair (Lin et al., 2014). Meanwhile, during heart repair fibroblasts expand and become myofibroblasts that assist in the repair of the infarct region, but if they do so excessively tissue fibrosis and scar formation occur (Moore-Morris et al., 2014).

Owing to technical challenges, the contribution of cell proliferation of individual cell types to disease progression remains largely unexplored, even though such insight could be

[1]The State Key Laboratory of Cell Biology, CAS Center for Excellence on Molecular Cell Science, Shanghai Institute of Biochemistry and Cell Biology, Chinese Academy of Sciences, University of Chinese Academy of Sciences, Shanghai 200031, China. [2]Key Laboratory of Nutrition and Metabolism, Institute for Nutritional Sciences, Shanghai Institutes for Biological Sciences, University of Chinese Academy of Sciences, Chinese Academy of Sciences, Shanghai 200031, China. [3]School of Life Science and Technology, ShanghaiTech University, Shanghai 201210, China. [4]Bioscience Cardiovascular, Research and Early Development, Cardiovascular, Renal and Metabolism (CVRM), BioPharmaceuticals R&D, AstraZeneca, Gothenburg 40530, Sweden. [5]Key Laboratory of Regenerative Medicine of Ministry of Education, Jinan University, Guangzhou 510632, China. [6]Shanghai Engineering Research Center for Model Organisms, Shanghai Model Organisms Center, Inc. (SMOC), Shanghai 201203, China. [7]The Collaborative Innovation Center for Cardiovascular Disease Translational Medicine, Nanjing Medical University, Nanjing 211100, China. [8]Key Laboratory of Cardiovascular and Cerebrovascular Medicine, Collaborative Innovation Center for Cardiovascular Disease Translational Medicine, Nanjing Medical University, Nanjing 211100, China. [9]State Key Laboratory of Cardiovascular Disease, Fuwai Hospital, National Center for Cardiovascular Disease, Chinese Academy of Medical Sciences and Peking Union Medical College, Beijing 10037, China. [10]Institute for Stem Cell and Regeneration, Chinese Academy of Sciences, Beijing 100101, China.
*These authors contributed equally to this work

‡Author for correspondence (zhoubin@sibs.ac.cn)

W.Y., 0000-0001-6288-4452; B.Z., 0000-0001-5278-5522

Received 19 August 2019; Accepted 10 January 2020

Development (2020) 147, dev183830. doi:10.1242/dev.183830

valuable. For example, in addition to the cell-autonomous role of cell proliferation, manipulation of the proliferation of one cell type could also provide a unique opportunity to understand the behavior of other cell types in the disease or repair process. Previous studies in liver regeneration showed that biliary epithelial cells or ductal cells do not differentiate into new hepatocytes after injury, and hepatocytes proliferate by themselves to generate new hepatocytes after liver injury (Chu et al., 2011; Malato et al., 2011; Schaub et al., 2014; Tarlow et al., 2014; Yanger et al., 2014). However, a recent study reported that impaired hepatocyte proliferation could induce the conversion of biliary epithelial cells to new hepatocytes (Raven et al., 2017; Deng et al., 2018), indicating that manipulation of cell proliferation could advance our understanding of cell plasticity and tissue regeneration. Therefore, manipulation of cell proliferation may provide a unique approach to understanding the role of lineage expansion of a single cell type in the context of a whole organism's response to injury, while also unraveling the underlying cellular plasticity.

To generate a genetic system that allows inducible cell cycle arrest in a tissue-specific manner, we used controlled expression of the cell cycle inhibitor gene *p21* (*Cdkn1a*) for cell proliferation inhibition (Carlson et al., 2008; Raven et al., 2017). To achieve tissue specificity, we employed a Cre-loxP recombination system to target p21 overexpression, while also expressing GFP to mark such cells (ip21-GFP system). We found that p21-overexpressing cells did not proliferate during homeostasis, disease, or after injury. Further, to facilitate the use of ip21-GFP in combination with another cell lineage tracing system, we also generated a second ip21-GFP system that was responsive to Dre-rox recombination and orthogonal to Cre-loxP system (Anastassiadis et al., 2009). Here, we present examples of how these tools could improve our understanding of the role of cell proliferation and non-cell-autonomous effects on cell fate plasticity during disease and tissue regeneration.

RESULTS

Generation and characterization of an inducible p21-GFP genetic system

To allow Cre-mediated gene expression, we generated a *R26-p21-GFP* allele by homologous recombination using a CRISPR/Cas9 strategy (Fig. 1A). GFP was linked with p21 by a self-cleaving 2A peptide so that GFP activity indicated p21 expression in the targeted cells (Fig. 1A). To characterize the *R26-p21-GFP* mouse line, we first crossed it with a Cre line for the cardiac fibroblast study. Namely, we used a fibroblast-specific CreER line, *Col1a2-CreER* (Fig. 1B), which is specifically expressed in fibroblasts in the developing heart (Fig. S1). We then crossed *Col1a2-CreER* mice with *R26-p21-GFP* mice to generate double-positive mice for subsequent experiments. Tamoxifen treatment of these mice at postnatal day (P) 3 induces Cre-loxP-mediated Stop cassette removal and subsequent p21-GFP expression in Col1a2$^+$ fibroblasts (Fig. 1C). As a control reporter line, we used *R26-tdTomato* (Madisen et al., 2010) for the study of *Col1a2-CreER*-labeled cells. Whole-mount fluorescence of P8 hearts showed efficient GFP or tdTomato expression in *Col1a2-CreER;R26-p21-GFP* and *Col1a2-CreER;R26-tdTomato* tissues, respectively (Fig. 1D). Immunostaining for GFP (surrogate for p21 expression) and PDGFRa (a fibroblast marker) in *Col1a2-CreER;R26-p21-GFP* heart sections showed that the majority of PDGFRa$^+$ cells co-expressed GFP (Fig. 1E).

We also detected highly efficient labeling by *Col1a2-CreER;R26-tdTomato* (Fig. 1E). Quantification revealed that 89.84±1.47% and 93.32±1.84% of PDGFRa$^+$ fibroblasts were labeled in *Col1a2-CreER;R26-p21-GFP* and *Col1a2-CreER;R26-tdTomato* hearts, respectively (Fig. 1F). There was negligible reporter activity in both groups in the vehicle-treated controls (Fig. 1F). Immunostaining for GFP and p21 on *Col1a2-CreER;R26-p21-GFP* showed robust p21 expression in GFP$^+$ cells (Fig. 1G), whereas p21 was not detected in tdTomato$^+$ fibroblasts in *Col1a2-CreER;R26-tdTomato* hearts (Fig. 1H). We also confirmed that a subset of PDGFRa$^+$ fibroblasts expressed p21 in heart sections from *Col1a2-CreER;R26-p21-GFP* mice (Fig. 1I). p21 expression was also detected in subsets of cardiomyocytes in both groups (Fig. S2). These data indicate that the *R26-p21-GFP* allele responded to Cre specifically and efficiently in fibroblasts, which was comparable to a conventional reporter.

To test functionally whether overexpression of p21 inhibits fibroblast proliferation, we stained tissue sections for Ki67 (Mki67) and found that GFP$^+$ fibroblasts in heart sections from *Col1a2-CreER;R26-p21-GFP* mice did not express Ki67, while a subset of tdTomato$^+$ fibroblasts in samples from *Col1a2-CreER;R26-tdTomato* mice did express Ki67 (Fig. 1J). Additionally, immunostaining for 5-ethynyl-2′-deoxyuridine (EdU) and GFP in heart sections from *Col1a2-CreER;R26-p21-GFP* mice showed no EdU incorporation in GFP$^+$ fibroblasts, whereas EdU was readily detected in non-fibroblast lineages, such as cardiomyocytes and endothelial cells (Fig. S3). As a control, EdU was readily detected in tdTomato$^+$ fibroblasts of hearts from *Col1a2-CreER;R26-tdTomato* mice (Fig. 1K). Quantification showed that 11.73±1.27% of fibroblasts incorporated EdU in hearts from *Col1a2-CreER;R26-tdTomato* mice, but almost no incorporation was observed in hearts from *Col1a2-CreER;R26-p21-GFP* mice (Fig. 1L). These data demonstrate that *R26-p21-GFP* could be used to inhibit proliferation of a specific cell lineage, such as fibroblasts (Fig. 1M).

Inhibition of fibroblast proliferation reduces scar formation after myocardial infarction

We next functionally tested whether inhibition of fibroblast proliferation could have any significant impact on tissue fibrosis after myocardial infarction (MI). We ligated the left anterior descending coronary artery in mice to induce MI at 2 weeks after tamoxifen treatment, and collected the hearts for analysis at 3 and 7 days following MI surgery (Fig. 2A). Hearts from *Col1a2-CreER;R26-p21-GFP* mice showed less collagen production compared with those from *Col1a2-CreER;R26-tdTomato* mice after MI injury (Fig. 2B). Sirius Red staining to measure the degree of fibrosis showed a significantly lower amount of tissue fibrosis in the *R26-p21-GFP* group compared with the *R26-tdTomato* group (Fig. 2C).

We then performed immunostaining for EdU and GFP or tdTomato on heart sections and found almost no detectable EdU$^+$GFP$^+$ fibroblasts in hearts from *Col1a2-CreER;R26-p21-GFP* mice, but a substantial number of EdU$^+$tdTomato$^+$ fibroblasts in hearts from *Col1a2-CreER;R26-tdTomato* mice at both 3 and 7 days following MI (Fig. 2D). Quantitatively, we found that whereas 13.39±1.76% and 2.54±0.52% of fibroblasts incorporated EdU at day 3 and 7 after MI, respectively, in the infarct regions of the hearts from *Col1a2-CreER;R26-tdTomato* mice, only 0.075±0.020% and 0.051±0.011% of fibroblasts incorporated EdU at day 3 and 7 after MI, respectively, in the infarct regions of hearts from *Col1a2-CreER;R26-p21-GFP* mice (Fig. 2E). Further, we found that most of the EdU$^+$ cells in the hearts of *Col1a2-CreER;R26-p21-GFP* mice were VE-cadherin (VE-cad; Cdh5)$^+$ endothelial cells or CD45 (PTPRC)$^+$ hematopoietic cells in the infarcted regions (Fig. 2F,G). We also detected Ki67$^+$tdTomato$^+$ fibroblasts in the *R26-tdTomato* group, but Ki67$^+$GFP$^+$ fibroblasts were not detected in the *R26-p21-GFP* group (Fig. 2H,I).

To validate this finding further, we collected hearts at 28 days after MI, the stage at which most stable scars form. We stained

Development (2020) 147, dev183830. doi:10.1242/dev.183830

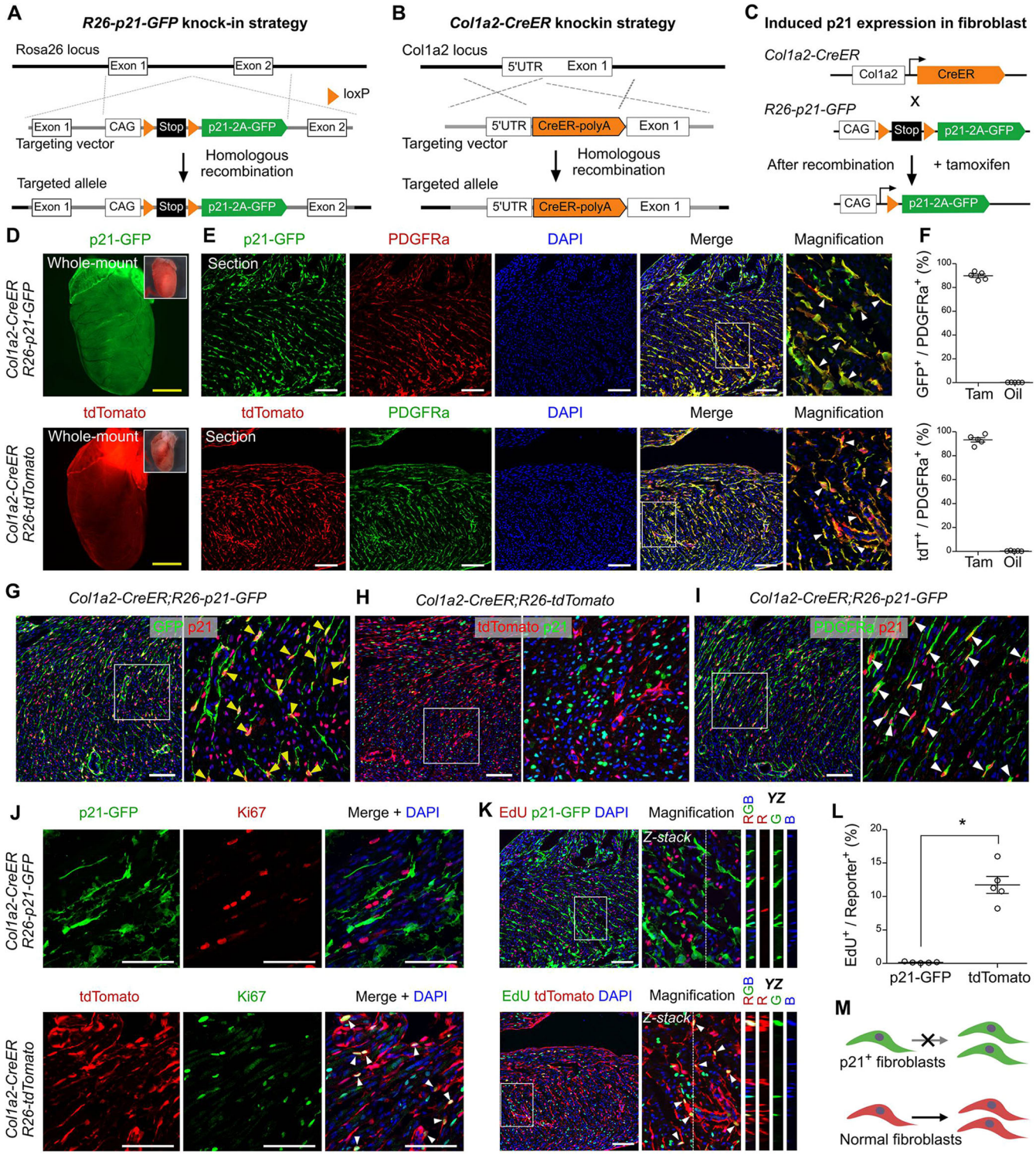

Fig. 1. Cell proliferation inhibited by induced expression of p21 in fibroblasts. (A,B) Schematic showing the generation of *R26-p21-GFP* (A) and *Col1a2-CreER* alleles (B) by homologous recombination. (C) Schematic indicating the experimental strategy. After mating, p21 and GFP are simultaneously expressed in fibroblasts after Cre-loxP recombination induced by tamoxifen. (D,E) Whole-mount fluorescence images (D) and immunostaining for p21-GFP or tdTomato and the fibroblast cell marker PDGFRa (E) of hearts from *Col1a2-CreER;R26-p21-GFP* mice and *Col1a2-CreER;R26-tdTomato* controls. Arrowheads indicate labeled cells. Insets in D show brightfield images of the same hearts. (F) Quantification of the percentage of PDGFRa$^+$ cells expressing GFP or tdTomato. Data are mean±s.e.m.; n=5. (G,H) Immunostaining for p21 and GFP (G) or tdTomato (H) on heart sections from *Col1a2-CreER;R26-p21-GFP* or *Col1a2-CreER;R26-tdTomato* mice. Yellow arrowheads indicate p21$^+$GFP$^+$ cells (G). (I) Immunostaining for p21 and PDGFRa on heart sections from *Col1a2-CreER;R26-p21-GFP* mice. White arrowheads indicate p21$^+$PDGFRa$^+$ fibroblasts. (J,K) Immunostaining for Ki67 and p21-GFP (J, top) or tdTomato (J, bottom) and immunostaining for EdU and p21-GFP (K, top) or tdTomato (K, bottom) on heart sections from *Col1a2-CreER;R26-p21-GFP* or *Col1a2-CreER;R26-tdTomato* mice. *YZ* indicates signals from dotted lines on *z*-stack images. Arrowheads indicate Ki67$^+$ fibroblasts or EdU$^+$ fibroblasts. (L) Quantification of the percentage of p21-GFP$^+$ or tdTomato$^+$ fibroblasts that are EdU$^+$. Data are mean±s.e.m.; n=5; *P<0.05 by Student's t-test. (M) Diagram showing proliferation in normal fibroblasts but not in p21$^+$ fibroblasts. In E,G-I,K, boxed areas are shown at higher magnification in panels to the right. Scale bars: 1 mm (yellow); 100 µm (white).

Development (2020) 147, dev183830. doi:10.1242/dev.183830

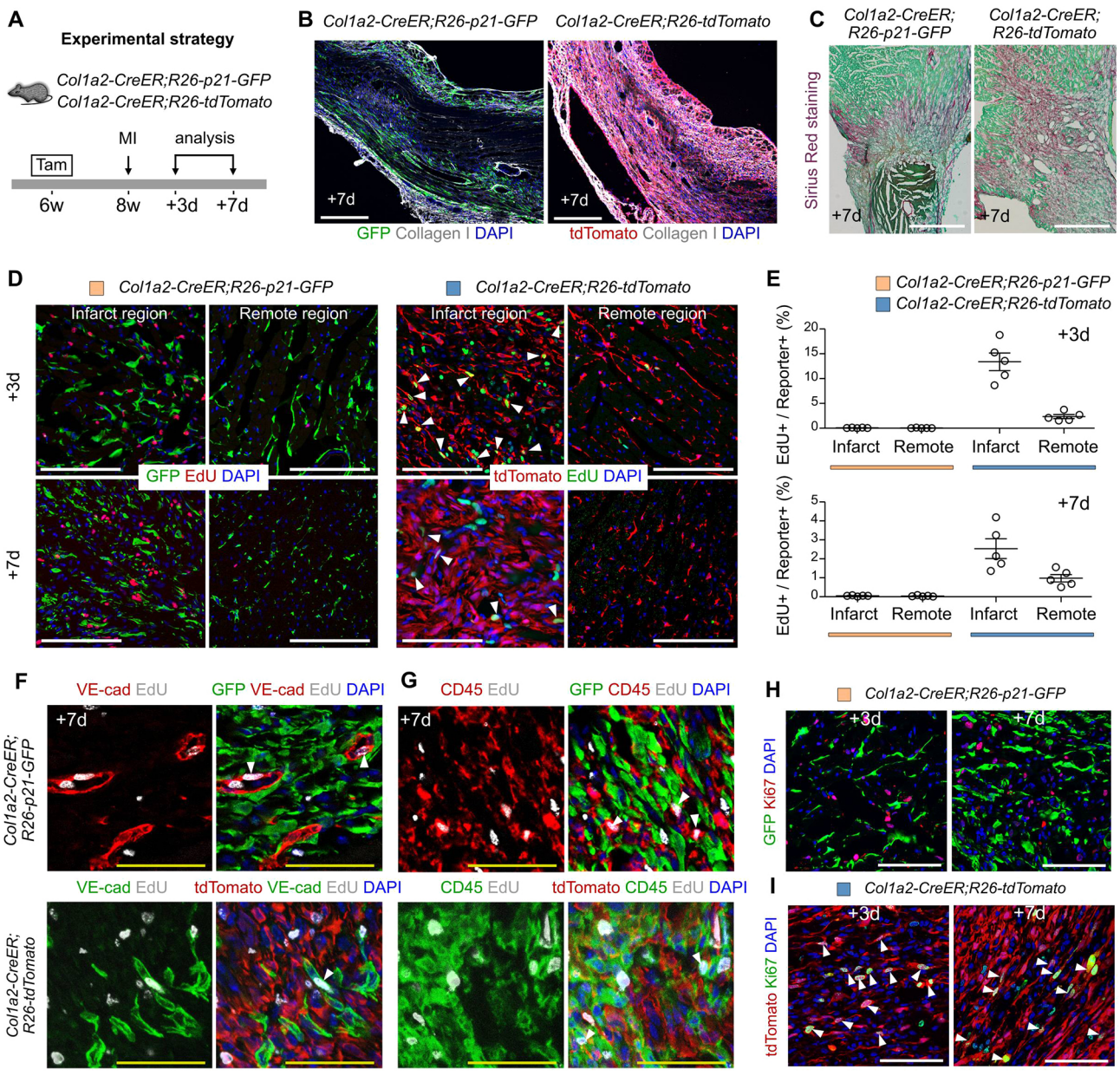

Fig. 2. Inhibition of fibroblast proliferation reduces scar formation after myocardial infarction. (A) Schematic showing the experimental strategy for myocardial infarction (MI). d, day; w, week. (B) Immunostaining for collagen I and GFP or tdTomato on heart sections. (C) Sirius Red staining on MI heart sections from *Col1a2-CreER;R26-p21-GFP* or *Col1a2-CreER;R26-tdTomato* mice. (D,E) Immunostaining for EdU and GFP or tdTomato on heart sections (D) and quantification of the percentage of GFP$^+$ or tdTomato$^+$ fibroblasts that are EdU$^+$ in infarct or remote regions of hearts at day 3 or 7 after MI (E) from *Col1a2-CreER; R26-p21-GFP* or *Col1a2-CreER;R26-tdTomato* mice. Data are mean±s.e.m.; *n*=5. (F,G) Immunostaining for GFP, EdU and VE-cad or CD45 on *Col1a2-CreER; R26-p21-GFP* MI heart sections and immunostaining for tdTomato, EdU and VE-cad or CD45 on *Col1a2-CreER;R26-tdTomato* MI heart sections. Arrowheads indicate EdU$^+$VE-cad$^+$ endothelial cells (F) and EdU$^+$CD45$^+$ hematopoietic cells (G). (H,I) Immunostaining for Ki67 and GFP (H) or tdTomato (I) on MI heart sections. Arrowheads indicate Ki67$^+$ fibroblasts. Scale bars: 100 µm (white); 50 µm (yellow).

PDGFRa and GFP or tdTomato on *Col1a2-CreER;R26-p21-GFP* or *Col1a2-CreER;R26-tdTomato* heart sections, respectively, and showed that both GFP and tdTomato were colocalized with the fibroblast cell marker (Fig. 3A). There was a noticeable reduction of GFP$^+$ fibroblasts compared with tdTomato$^+$ fibroblasts in the infarcted region of MI hearts (Fig. 3A). We also observed a significant increase of coronary blood vessels in the infarcted regions of *Col1a2-CreER;R26-p21-GFP* hearts compared with *Col1a2-CreER;R26-tdTomato* hearts (Fig. 3B), indicating that inhibition of fibroblast proliferation promoted neovascularization of injured myocardium. With more blood vessel supply, the area of surviving myocardium in the infarcted region of *Col1a2-CreER;R26-p21-GFP* was significantly greater than that of *Col1a2-CreER;R26-tdTomato* (Fig. 3C). Sirus Red staining on MI heart sections confirmed decreased scar formation in *Col1a2-CreER;R26-p21-GFP* hearts compared with littermate controls (Fig. 3D,E). Importantly, reduced scar formation was associated with improved heart function, as evaluated by echocardiography (Fig. 3F). These data suggest that inhibition of fibroblast proliferation significantly reduced scar formation and promoted neovascularization and cardiomyocyte survival.

Development (2020) 147, dev183830. doi:10.1242/dev.183830

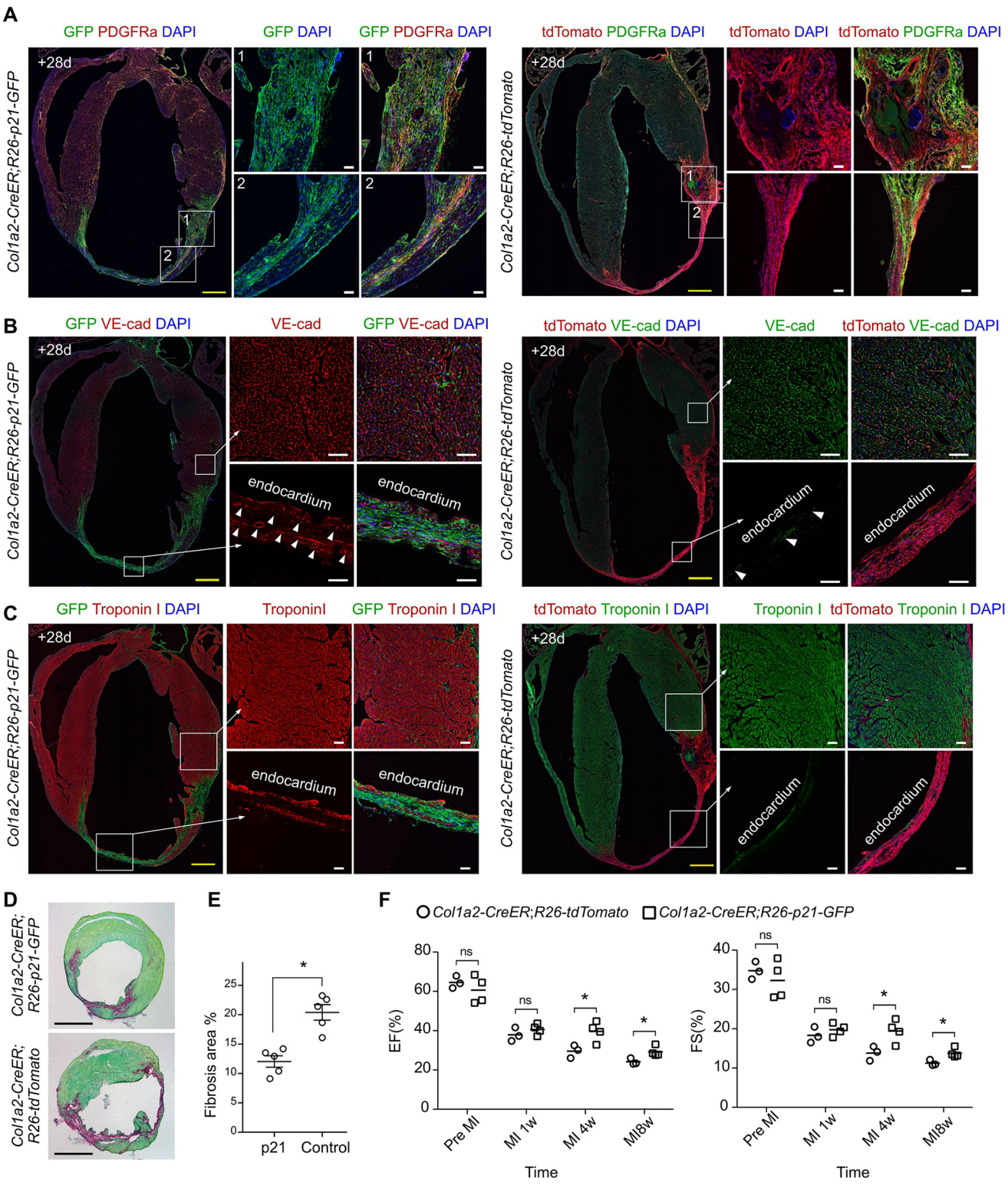

Fig. 3. Inhibition of fibroblast proliferation reduces scar formation and promotes neovascularization after myocardial infarction. (A) Immunostaining for PDGFRa and GFP or tdTomato on *Col1a2-CreER;R26-p21-GFP* or *Col1a2-CreER;R26-tdTomato* heart sections, respectively, at 28 days after MI. Numbered panels show higher magnifications of the respective boxed areas on the left. (B) Immunostaining for VE-cad and GFP or tdTomato on MI heart sections from *Col1a2-CreER;R26-p21-GFP* or *Col1a2-CreER;R26-tdTomato* mice, respectively. Arrowheads indicate VE-cad^{+} coronary vessels. (C) Immunostaining for TNNI3 (troponin I) and GFP or tdTomato on MI heart sections from *Col1a2-CreER;R26-p21-GFP* or *Col1a2-CreER;R26-tdTomato* mice, respectively. (D) Sirius Red staining on *Col1a2-CreER;R26-p21-GFP* or *Col1a2-CreER;R26-tdTomato* heart sections at 28 days after MI injury. (E) Quantification of the percentage of fibrosis area in the MI heart sections. Data are mean±s.e.m.; n=5; *P<0.05 by Student's t-test. (F) Echocardiography was performed in *Col1a2-CreER;R26-p21-GFP* mice and *Col1a2-CreER;R26-tdTomato* controls on week 1 before MI (Pre MI) and week 1, week 4, week 8 after MI to determine ejection fraction (EF) as well as fraction shortening (FS). Data are mean±s.e.m.; n=3-4; *P<0.05 by Student's t-test. ns, no significance. Scale bars: 1 mm (yellow); 100 µm (white); 200 µm (black).

Development (2020) 147, dev183830. doi:10.1242/dev.183830

Independently, we induced inhibition of fibroblast proliferation in a myocardial ischemia-reperfusion model using ip21-GFP mice (Fig. S4). We found that overexpression of p21 in fibroblasts inhibited their proliferation and ameliorated tissue fibrosis after myocardial ischemia-reperfusion injury (Fig. S4). Taken together, these data show that inhibition of fibroblast proliferation through p21 overexpression reduces tissue fibrosis and scar formation.

Inhibition of hepatocyte proliferation induced by p21-GFP

To show application of the ip21-GFP system in another context, we studied its effect on inhibition of hepatocyte proliferation in liver homeostasis or injury. We crossed *Alb-CreER* mice, which selectively express CreER in hepatocytes and epithelia cells of kidney via the albumin promoter (Fig. S5), with those harboring the *R26-p21-GFP* reporter. We then induced p21-GFP expression in Alb^+ hepatocytes by tamoxifen (Fig. 4A). To detect hepatocyte proliferation, we collected livers from 4-week-old mice and analyzed them for GFP expression. We detected GFP signal in the livers of the tamoxifen-treated, but not vehicle-treated, *Alb-CreER; R26-p21-GFP* mice (Fig. 4B). These GFP^+ cells expressed a high level of p21 in mice treated with tamoxifen whereas no $p21^+$ cells were detected in mice after vehicle treatment (Fig. 4C, Fig. S6A). Quantitative RT-PCR showed significantly higher *p21* expression in hepatocytes isolated from mice treated with tamoxifen compared with vehicle-treated mice (Fig. 4D).

To verify that the expression of p21-GFP was specific to hepatocytes in liver, we co-stained for GFP and the hepatocyte marker HNF4a or the biliary epithelial cell marker CK19 (Krt19) on liver sections, and found that hepatocytes, but not biliary epithelial cells, express GFP (Fig. 4E,F). To test functionally whether the overexpression of p21-GFP inhibits hepatocyte proliferation, we stained liver sections for GFP and Ki67 (Fig. 4G). We found both $Ki67^+$ hepatocytes (larger, round nuclei; Fig. 4G, arrowheads) and $Ki67^+$ non-hepatocytes (smaller, irregularly shaped nuclei; Fig. 4G, arrows) in the vehicle-treated group. In contrast, we detected Ki67 expression in GFP^- non-hepatocytes but not in GFP^+ hepatocytes in liver sections of tamoxifen-treated mice (Fig. 4G). Quantitative data showed that although there was no significant difference in the number of proliferating non-hepatocytes between vehicle- and tamoxifen-treated samples, the number of proliferating hepatocytes per field was markedly different between the two groups (Fig. 4H).

At the adult stage (8 weeks of age and later), most hepatocytes do not proliferate during tissue homeostasis, but they do proliferate more prominently after injury (Pu et al., 2016). Thus, we next explored whether the ip21-GFP system in the adult liver would have any effect on hepatocyte proliferation after liver injury. We first induced carbon tetrachloride (CCl_4)-mediated liver injury at 2 weeks after tamoxifen or oil treatment and then collected samples 48 h later to check the response of hepatocytes to acute injury (Fig. 4I). Immunostaining for GFP and Ki67 on liver sections from the oil-treated group showed that hepatocytes responded robustly to injury by boosting the cell cycle at an extremely high level, as 25.14±1.91% of hepatocytes expressed Ki67 (Fig. 4J,K). However, we could barely detect any proliferating hepatocytes after injury in the tamoxifen-treated group (Fig. 4J,K). In the same sections, we also detected $Ki67^+$ cells that were GFP^-, indicating that non-hepatocytes proliferate in response to injury in *Alb-CReER; R26-p21-GFP* mice treated with tamoxifen (Fig. 4J). In the sham controls, we detected very few $Ki67^+$ hepatocytes in the oil-treated group and none in the tamoxifen-treated group (Fig. S6B). These data demonstrate that the ip21-GFP system could be used to specifically inhibit hepatocyte proliferation during both tissue homeostasis and in response to injury (Fig. 4L).

We next exposed *Alb-CReER;R26-p21-GFP* mice to a chronic liver injury model by treating them for 3 weeks with a 3,5-diethoxycarbonyl-1,4-dihydrocollidine (DDC)-containing diet (Fig. S7A). In both normal and DDC diets, tamoxifen treatment induced robust p21-GFP expression in the liver (Fig. S7B). Whereas all examined $HNF4a^+$ hepatocytes in the normal-diet group were GFP^+, we noticed a subset of $HNF4a^+$ hepatocytes that were GFP^- in the DDC-fed group (Fig. S7C). Noticeably, most of these $HNF4a^+GFP^-$ cells were restricted to the peri-portal region, where they were closely associated with $CK19^+$ biliary epithelial cells (Fig. S7C). Immunostaining for GFP, E-cadherin (E-cad, a peri-portal hepatocyte marker; also known as Cdh1) and glutamine synthetase (GS, a peri-central hepatocyte marker) on liver sections from DDC-treated mice showed that a subset of GFP^- hepatocytes were present in the peri-portal regions (Fig. S7D).

We never observed the appearance of GFP^- hepatocyte clusters in the normal-diet group (Fig. S7D). Functionally, GFP^- hepatocytes, but not GFP^+ hepatocytes, express Ki67 in the peri-portal regions in the livers of DDC-fed mice (Fig. S7E). Consistent with this observation, we found that GFP^+ hepatocytes, but not GFP^- hepatocytes, expressed p21 (Fig. S7F). These GFP^- hepatocytes may emerge from a limited number of unlabeled pre-existing hepatocytes. However, it is also possible that inhibition of hepatocyte proliferation in chronic injury may induce a new hepatocyte generation from other cell lineages, such as has been previously reported for biliary epithelial cells (BECs) (Raven et al., 2017).

Generation of the *R26-rox-p21-GFP* system for inhibition of cell proliferation

Cre-loxP has been widely used and the ip21-GFP system would be compatible with many existing Cre-based tools in current use. However, to inhibit the proliferation of one cell lineage at the same time as genetically tracing or manipulating another cell lineage, an alternative genetic system is needed in addition to the present Cre-loxP system. A previous report indicated that Dre-rox and Cre-loxP were two orthogonal recombination systems, and they could be used simultaneously for more precise evaluation of cell fate plasticity and gene function *in vivo* (Anastassiadis et al., 2009; Hermann et al., 2014; He et al., 2017b; Pu et al., 2018). We therefore generated a Dre-rox-induced p21-GFP expression tool based on a *R26-rox-p21-GFP* allele (Fig. 5A), which responds to Dre recombinase and expresses p21-GFP upon AAV8-TBG (human thyroid hormone-binding globulin; also known as SERPINA7)-Dre virus treatment (Fig. 5B).

We did not detect any GFP signal in *R26-rox-p21-GFP* mice with AAV8-control virus treatment (Fig. 5B), indicating no leakiness of the *R26-rox-p21-GFP* allele in the absence of Dre expression. Also, given the serotype of the AAV vector, we found that AAV8-TBG-Dre specifically targeted rox sites in hepatocytes (Fig. S8). Immunostaining showed that almost all $HNF4a^+$ hepatocytes were GFP^+ after Dre virus treatment, whereas hepatocytes were GFP^- in livers of mice treated with a control virus (Fig. 5C,D). We also found that p21 was expressed in almost all GFP^+ hepatocytes in liver samples from Dre, but not control, virus-treated mice (Fig. 5E). Although the proliferation of adult hepatocytes was extremely low, we did detect $Ki67^+$ hepatocytes in AAV8-control treated mice (Fig. 5F). However, we never detected $Ki67^+$ hepatocytes in Dre virus-treated mice out of 65 liver sections from five mice examined (Fig. 5F).

We next exposed the mice to CCl_4 treatment and collected samples for analysis of cell proliferation (Fig. 5G). CCl_4 mainly induced acute

Development (2020) 147, dev183830. doi:10.1242/dev.183830

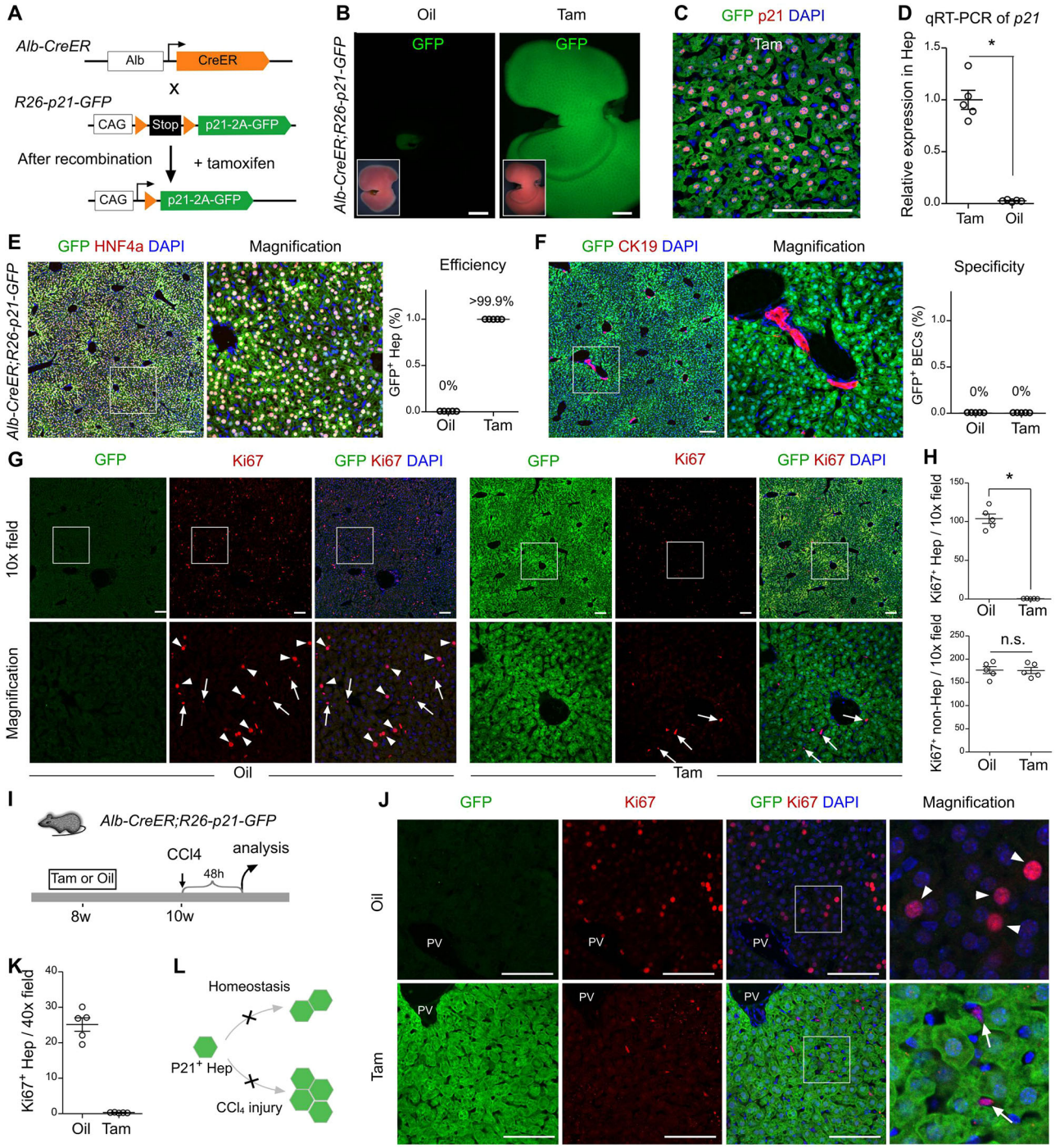

Fig. 4. Specific inhibition of hepatocyte proliferation by induced p21 expression. (A) Schematic showing Cre-loxP recombination-mediated p21 and GFP expression in Alb$^+$ hepatocytes. (B) Whole-mount fluorescence views of livers from *Alb-CreER;R26-p21-GFP* mice treated with tamoxifen (Tam) or oil. Insets show bright-field images. (C) Immunostaining for GFP and p21 in *Alb-CreER;R26-p21-GFP* mouse treated with Tam. (D) qRT-PCR of *p21* expression in isolated hepatocytes (Hep). Data are mean±s.e.m.; n=5; *P<0.05. (E,F) Immunostaining for GFP and HNF4a (E, left) or CK19 (F, left) on liver sections from *Alb-CreER;R26-p21-GFP* mice, and quantification of the percentage of GFP$^+$ cells in HNF4a$^+$ hepatocytes (Hep; E, right) or CK19$^+$ biliary epithelial cells (BECs; F, right). Data are mean±s.e.m.; n=5. (G) Immunostaining for the proliferation marker Ki67 and the reporter GFP on liver sections. Arrowheads indicate Ki67$^+$ hepatocytes; arrows indicate Ki67$^+$ non-hepatocytes. (H) Quantification of the number of Ki67$^+$ Hep or non-Hep cells in each field. Data are mean±s.e.m.; n=5; *P<0.05; n.s., non-significant. (I) Schematic indicating the experimental design for the liver injury study. (J) Immunostaining for GFP and Ki67 on liver sections. Arrowheads indicate Ki67$^+$ hepatocytes; arrows indicate Ki67$^+$ non-Hep cells. PV, portal vein. (K) Quantification of Ki67$^+$ hepatocytes per field. (L) Diagram illustrating no proliferation of p21$^+$ hepatocytes during liver homeostasis or after injury. Scale bars: 2 mm (B); 100 µm (C,E-G,J). Each image is representative of five individual biological samples. Boxed areas are shown at higher magnification to the right or below.

injury in the peri-central region (Fig. 5H), which would lead to peri-central hepatocyte death and induction of proliferation of peri-portal hepatocytes as a compensatory mechanism (Pu et al., 2016). Immunostaining for GFP, HNF4a and CK19 showed hepatocyte death in the peri-central region of AAV8-control- or AAV8-Dre-treated mouse livers (Fig. 5I). We detected robust hepatocyte

Development (2020) 147, dev183830. doi:10.1242/dev.183830

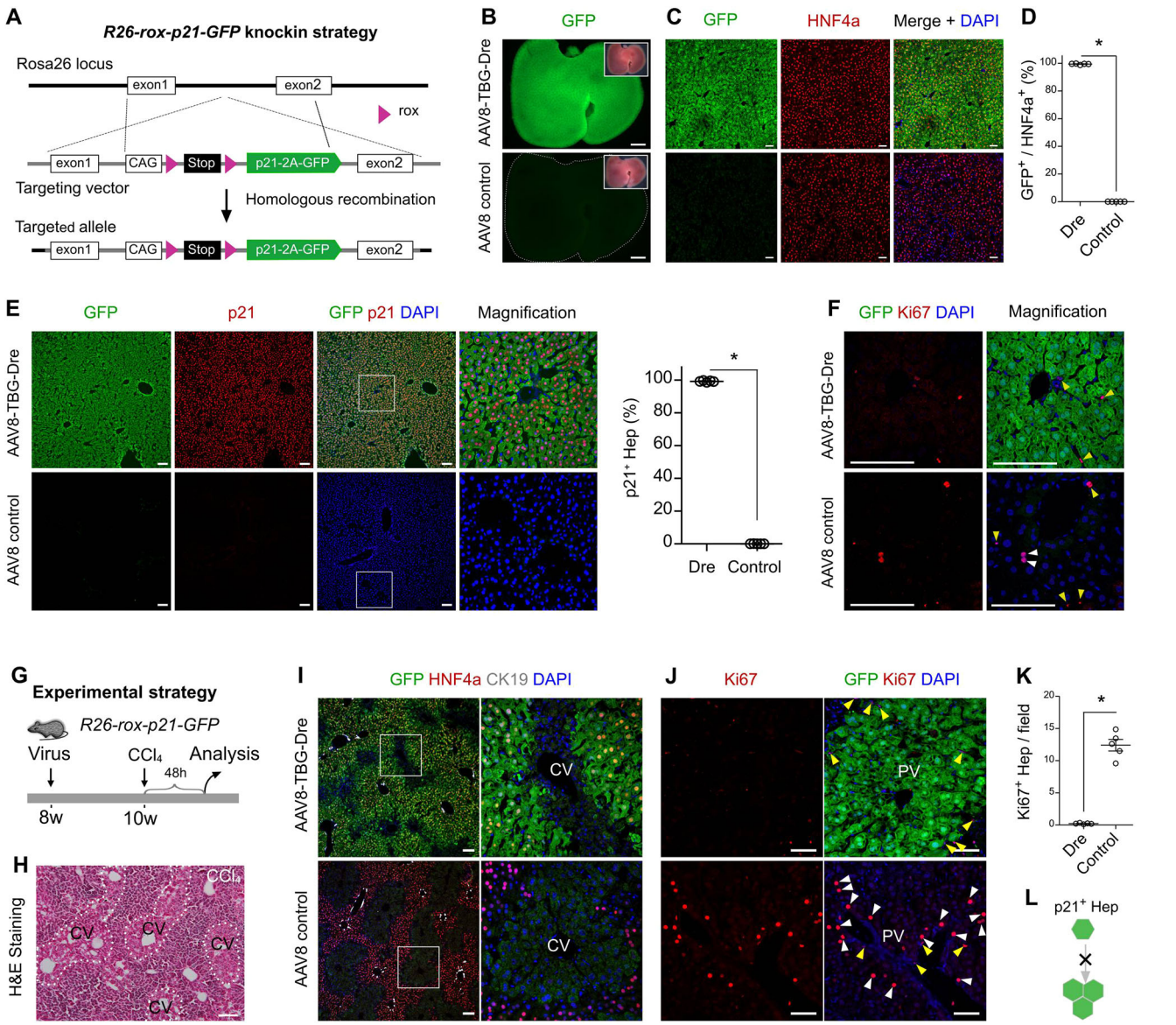

Fig. 5. Generation of Dre-rox-induced p21 expression mouse allele. (A) Schematic showing the knock-in strategy for the generation of the *R26-rox-p21-GFP* allele using CRISPR/Cas9 by homologous recombination. (B) Whole-mount fluorescence images of adult liver from *R26-rox-p21-GFP* mice treated with AAV8-TBG-Dre or control AAV8 virus. Insets show brightfield images of the same livers. (C) Immunostaining for GFP and HNF4a on liver sections from *R26-rox-p21-GFP* mice treated with Dre or control virus. (D) Quantification of the percentage of GFP$^+$ hepatocytes. Data are mean±s.e.m.; n=5, *P<0.05. (E) Immunostaining for GFP and p21 on liver sections in Dre- or control virus-treated mice (left), and quantification of the percentage of hepatocytes expressing p21 (right). Data are mean±s.e.m.; n=5, *P<0.05. (F) Immunostaining for Ki67 and GFP on liver sections. White arrowheads indicate Ki67$^+$ hepatocytes; yellow arrowheads indicate Ki67$^+$ non-hepatocytes. (G) Schematic illustrating the experimental strategy for acute liver injury model. (H) Hematoxylin & Eosin staining of injured peri-central vein regions (dotted line) induced by CCl4. (I) Immunostaining for GFP, HNF4a and CK19 on liver sections from Dre- or control virus-treated mice. CV, central vein. (J) Immunostaining for Ki67 and GFP in liver sections. PV, portal vein. White arrowheads indicate Ki67$^+$ hepatocytes; yellow arrowheads indicate Ki67$^+$ non-hepatocytes. (K) Quantification of the percentage of hepatocytes expressing Ki67 in control or Dre groups. Data are mean±s.e.m.; n=5; *P<0.05. (L) Diagram showing inhibition of hepatocyte proliferation by p21 after CCl4-induced liver injury. Scale bars: 2 mm (B); 100 µm (C,E,F,H-J). Each image is representative of five individual biological samples. Boxed areas are shown at higher magnification to the right.

proliferation in the peri-portal region of AAV8-control- but not Dre virus-treated mice (Fig. 5J,K). These data demonstrate that the *R26-rox-p21-GFP* system could be used to inhibit cell proliferation in specific cell lineages targeted by Dre (Fig. 5L).

Inhibition of hepatocyte proliferation-induced conversion of BECs to hepatocytes

To test whether inhibition of the proliferation of one cell lineage can induce another cell lineage to trans-differentiate and compensate for the loss of the targeted cells, we induced chronic liver injury by DDC diet in *R26-rox-p21-GFP* mice (Fig. S9A). For both normal and DDC diet groups, AAV8-TBG-Dre treatment of *R26-rox-p21-GFP* mice led to efficient recombination in the liver (Fig. S9B). Immunostaining for GFP, HNF4a and CK19 on liver sections showed that hepatocytes in both peri-central and peri-portal regions were efficiently labeled by GFP (Fig. S9C). Immunostaining with the zonation markers E-cad and GS showed the efficient labeling (>99%) of hepatocytes in peri-portal and peri-central regions of the liver lobule (Fig. S9C). In *R26-rox-p21-GFP* mice fed the DDC diet, we detected clusters of prominent GFP$^-$ hepatocytes appearing

Development (2020) 147, dev183830. doi:10.1242/dev.183830

in the midst of GFP^+ hepatocytes (Fig. S9D). Many of these GFP^- clones were closely associated with BECs. These GFP^- hepatocytes expressed Ki67 but not p21, whereas their surrounding GFP^+ hepatocytes expressed p21 but not Ki67 (Fig. S9E,F).

These data suggest that p21-GFP expression in hepatocytes inhibited their proliferation, whereas $p21^-GFP^-$ hepatocytes emerge to proliferate as a clonal expansion to generate new hepatocytes during chronic liver injury. These proliferating GFP^- hepatocytes are likely derived from a very few pre-existing hepatocytes that have not been targeted by the Dre virus. It is also likely that hepatocyte inhibition spurs the potential of BECs to convert into hepatocytes during liver repair and regeneration. Both mechanisms may happen for generating new hepatocytes.

To address BEC-to-hepatocyte conversion directly, we combined the Dre-rox and Cre-loxP orthogonal systems to inhibit one cell lineage proliferation while simultaneously genetically tracing another cell lineage. Treating *R26-rox-p21-GFP;CK19-CreER; R26-tdTomato* mice with AAV8-TBG-Dre virus (Fig. 6A), we inhibited hepatocytes proliferation by the Dre-rox system and simultaneously induced CK19-CreER-mediated lineage tracing of BECs in the liver. Virtually all hepatocytes (i.e. $HNF4a^+$) expressed p21-GFP and 40.92±1.84% of BECs (i.e. $CK19^+$) were labeled with tdTomato in the liver (Fig. 6B-D). We fed mice for 4 weeks with the DDC diet, then switched them to a normal diet, and collected livers for analysis after 5 weeks' recovery (Fig. 6E).

A prominent cluster of a $tdTomato^+$ signal was detected in the AAV8-TBG-Dre-treated liver, compared with the AAV8-control-treated group (Fig. 6F). By immunostaining, we found clusters of $tdTomato^+HNF4a^+$ hepatocytes in the peri-portal regions (Fig. 6G), demonstrating that these hepatocytes were derived from pre-labeled BECs. No $tdTomato^+HNF4a^+$ hepatocytes were detected in the AAV8-control-treated mice (Fig. 6G). The BEC-derived hepatocytes expressed the peri-portal zonation marker E-cad but not the peri-central zonation marker GS (Fig. 6H,I). Although p21 was expressed in GFP^+ hepatocytes, we did not detect any p21 expression in $tdTomato^+$ hepatocytes (Fig. 6J). Further, we found that Ki67 was expressed in these $tdTomato^+$ hepatocytes, but not in GFP^+ hepatocytes (Fig. 6K). These data demonstrate that genetic inhibition of hepatocyte proliferation during chronic liver injury induces a BEC-to-hepatocyte conversion (Fig. 6L).

DISCUSSION

In this study, we generated an inducible genetic system to inhibit cell proliferation in a tissue-specific manner. We presented two examples of how this genetic approach could be used for studying the role of cell proliferation in tissue homeostasis, repair and regeneration. During MI many cell lineages, including endothelial cells, fibroblasts and cardiomyocytes, respond to injury by increasing their proliferation. Unravelling the specific role of the expansion of one cell type in the context of the whole-organ response is crucial for understanding the function of this expansion and also for potential therapeutic targets. It has been reported that ablation of myofibroblasts in the injured myocardium reduces collagen production and scar formation after MI (Kanisicak et al., 2016; Kaur et al., 2016). After MI, the resident pre-existing fibroblasts respond to hypoxic conditions and expand to form essentially all myofibroblasts (He et al., 2017a). As excessive myofibroblasts were a result of cell proliferation from pre-existing fibroblasts, we therefore used the ip21-GFP system to inhibit the fibroblast proliferation and excessive expansion, which resulted in a significant reduction of tissue fibrosis and scar formation. Of note, inhibition of fibroblast proliferation significantly promoted neovascularization, resulting in more cardiomyocyte survival in the infarcted region.

It has been proposed that facultative resident hepatic stem or progenitor cells contribute to new hepatocytes after injury in both fish and mice (Español-Suñer et al., 2012; Choi et al., 2014; He et al., 2014; Rodrigo-Torres et al., 2014). However, genetic lineage-tracing studies in mice indicate that pre-existing hepatocytes are the cellular source of new hepatocytes generated after injury (Schaub et al., 2014; Tarlow et al., 2014; Yanger et al., 2014). Rather than putative stem cell differentiation, adult hepatocytes are generated by self-duplication or proliferation (Chu et al., 2011; Malato et al., 2011). In chronic severe human liver diseases, hepatocyte proliferation was significantly impaired in the context of widespread hepatocyte senescence, indicative of p21 upregulation (Marshall et al., 2005; Richardson et al., 2007). However, the general injury models (e.g. hepatectomy, CCl_4, DDC or bile duct ligation) in mice stimulate rather than inhibit hepatocyte proliferation in the liver, which does not actually recapitulate human chronic liver injury conditions. To mimic human liver injury conditions in a mouse model, a recent study employed gene manipulation to inhibit hepatocyte proliferation in a combination of conventional liver injuries, and then found that cholangiocytes contribute to hepatocytes in this particular condition (Raven et al., 2017). Xie and colleagues also reported that the conversion of cholangiocytes to hepatocytes could occur in mouse after long-term severe liver injuries (Deng et al., 2018). The inhibition of hepatocytes therefore has relevant biological significance for the study of cell lineage plasticity in models of human liver diseases. These studies and ours also suggested that hepatocyte regeneration from biliary cells might occur in human chronic liver disease. Identifying the cellular sources of hepatocyte regeneration could provide insights for developing new therapeutic strategies.

We therefore generated an inducible Cre-loxP-based genetic tool for p21 overexpression to selectively inhibit cell proliferation in any cell type of interest (as long as a relevant Cre-driver is available). To prove the utility of this new system, we showed that *Alb-CreER*-mediated recombination results in highly efficient and specific overexpression of p21-GFP in hepatocytes, suppressing their proliferation both in homeostasis and after injury. Interestingly, we did observe a cluster of $p21^-$ hepatocytes appearing in the peri-portal regions after chronic injury and these cells were tightly associated with ductal cells. It is possible that very rare pre-existing $p21^-$ hepatocytes expand during injury. However, due to the restricted regions that associate with BECs in the peri-portal region, it is more likely these $p21^-$ hepatocytes were derived from $p21^-$ BECs after injury when hepatocyte proliferation is impaired (Raven et al., 2017).

In addition to the Cre-loxP recombination system, we also generated a Dre-rox-mediated p21-GFP expression genetic system. By comparing hepatocyte proliferation, we found that the *R26-rox-p21-GFP* system works as efficiently and specifically as *R26-p21-GFP* for suppressing cell proliferation. Because Cre-loxP and Dre-rox are two orthogonal recombination systems (He et al., 2017b), we then employed Dre-rox to inhibit hepatocyte proliferation by p21-GFP and simultaneously used *CK19-CreER;R26-tdTomato* alleles to trace BECs in the same liver. In such mice fed a DDC diet to induce chronic liver injury, we detected clusters of $tdTomato^+$ BECs-derived hepatocytes in the peri-portal regions. Of note, we also observed clusters of $tdTomato^-GFP^-$ in the same liver after injury. We observed that $tdTomato^+$ hepatocytes contributed to 0.22±0.021% of the liver by quantification of liver sections stained with tdTomato, GFP and HNF4a. This was partly due to the inefficiency of BEC labeling by *CK19-CreER* (~40%). We also

Development (2020) 147, dev183830. doi:10.1242/dev.183830

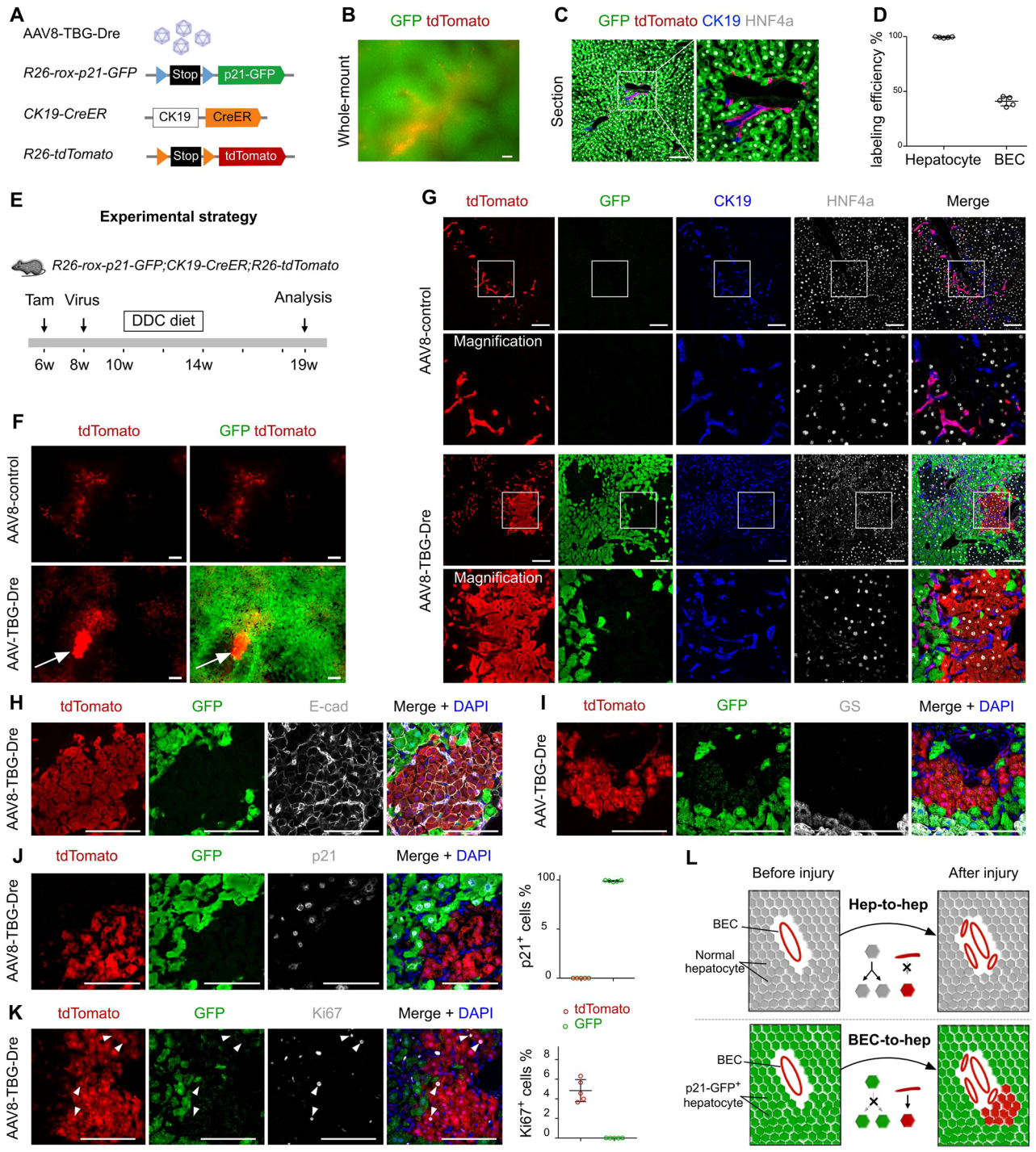

Fig. 6. BECs convert into new hepatocytes after inhibition of pre-existing hepatocytes proliferation. (A) Schematic showing the strategy for Dre-rox and Cre-loxP recombinations. (B) Whole-mount fluorescence image of *R26-rox-p21-GFP;CK19-CreER;R26-tdTomato* liver treated with a Dre virus. (C,D) Immunostaining for GFP, tdTomato, CK19 and HNF4a showing GFP$^+$ hepatocytes and tdTomato$^+$ BECs (C), and quantification of the labeling efficiency in hepatocytes or BECs (D). (E) Schematic showing the experimental strategy for DDC-induced liver injury. (F) Whole-mount fluorescence of livers from AAV8-control- or AAV8-TBG-Dre-treated mice. Arrows indicate a clone of tdTomato$^+$ hepatocytes. (G) Immunostaining for GFP, tdTomato, CK19 and HNF4a on liver sections from mice treated with AAV8-control or AAV8-TBG-Dre. (H,I) Left: Immunostaining for tdTomato, GFP, E-cad or GS on liver sections from mice treated with Dre virus. (J,K) Immunostaining for tdTomato, GFP and p21 (J) or Ki67 (K) on liver sections from mice treated with Dre virus (left). Arrowheads indicate Ki67$^+$tdTomato$^+$ hepatocytes. Right: Quantification of the percentage of tdTomato$^+$ or GFP$^+$ cells expressing p21 or Ki67. Data are mean±s.e.m.; *n*=5. (L) Cartoon image showing that BECs generate hepatocytes (hep) after injury when pre-existing hepatocytes proliferation is inhibited. Scale bars: 100 µm. Each image is representative of five individual biological samples. Boxed areas are shown at higher magnification to the right or below.

found that tdTomato$^-$GFP$^-$ hepatocytes accounted for 30.5±4.7% of all hepatocytes after DDC injury. The presence of a high proportion of tdTomato$^-$GFP$^-$ hepatocytes was attributed to incomplete genetic targeting by AAV8-TBG-Dre. Although the majority of pre-existing hepatocytes overexpress p21-GFP after Dre-rox recombination, the very small number of untargeted

Development (2020) 147, dev183830. doi:10.1242/dev.183830

hepatocytes (GFP^-) expands significantly during liver injury, maintaining GFP^- and exhibiting a lack of tdTomato expression. Owing to the presence of a subset of $p21^-GFP^-$ hepatocytes, the magnitude of lineage conversion from BECs to hepatocytes could be significantly reduced after liver injury. Improving the efficiency of AAV8-TBG-Dre virus infection or using the *Alb-ires-DreER* line would likely enhance the efficiency of hepatocyte proliferation inhibition, thereby promoting the levels of regeneration of hepatocytes from biliary cells.

A previous study revealed the hepatobiliary hybrid progenitor (HHyP) population in human fetal liver, which suggested the possibility that BECs express other lineage markers after stress (Segal et al., 2019). However, our genetic labeling was induced at 4 weeks before liver injury, so our labeled cells were BECs under normal conditions. It is less likely that we labeled the HHyP population during the time window when we administered the tamoxifen. Although the possible existence of a HHyP population during stress may represent a new interesting direction, our study does not focus on identification of a HHyP population in the adult liver under stress. Even so, our work provides an example of inhibition of one cell type by ip21-GFP leading to the cell-fate conversion of another cell lineage, indicating the non-cell-autonomous role of cell proliferation inhibition during chronic injury.

Taken together, our work provides two inducible genetic tools for inhibition of cell proliferation of specific cell lineages. Combination of *R26-p21-GFP* or *R26-rox-p21-GFP* with other genetic tools could further help elucidate both the cell-autonomous and non-cell-autonomous role of cell proliferation in development, disease and regeneration. We expect that dissecting the exact role of proliferation of one cell lineage will provide new insights into disease pathogenesis, while also uncovering potential new therapeutic targets for the treatment of disease and/or improving regenerative medicine.

MATERIALS AND METHODS

Mice

All mice studies were carried out in accordance with the guidelines in the Institutional Animal Care and Use Committee (IACUC) of the Institute for Nutritional Sciences and the Institute of Biochemistry and Cell Biology, Shanghai Institutes for Biological Sciences, Chinese Academy of Science. The *Alb-CreER*, *CK19-CreER*, *R26-tdTomato* and *R26-rox-tdTomato* mouse lines have been published previously (Barker et al., 2007; Madisen et al., 2010; Zhang et al., 2016; He et al., 2017b). *Col1a2-CreER*, *R26-p21-GFP* and *R26-rox-p21-GFP* mouse lines were generated by homologous recombination using CRISPR/Cas9 technology. For *Col1a2-CreER*, the cDNA encoding CreER was inserted into the translational start codon ATG of the *Col1a2* gene, followed by a polyadenylation sequence. For *R26-p21-GFP*, the cDNA encoding CAG-loxp-stop-loxp-p21-P2A-GFP was inserted into the *Rosa26* gene locus (between exon 1 and exon 2). A P2A peptide sequence was used to link the *p21* coding region and *GFP* cDNA, allowing translation of both p21 and GFP proteins. For the *R26-rox-p21-GFP* mouse line, the CAG-rox-stop-rox-p21-P2A-GFP cDNA was generated and inserted into the *Rosa26* locus as *R26-p21-GFP*. These mouse lines were generated by Shanghai Biomodel Organism Co., Ltd., Shanghai, China. All mice involved in studies were maintained on 129/C57BL6 and ICR mixed background. Animals received tamoxifen (Sigma-Aldrich, T5648) dissolved in corn oil at the indicated time. Adult mice received 0.1 mg tamoxifen per gram mouse body weight by oral gavage. Both male and female mice were included in the study.

Whole-mount fluorescence microscopy

Collected mouse tissues were fixed in 4% paraformaldehyde (PFA; Sigma-Aldrich) and placed on agar for whole-mount imaging and *z*-stack imaging using a Zeiss stereomicroscope (Axio Zoom V16).

Immunostaining

Immunostaining was performed as previously described. In detail, dissected tissues were fixed in 4% PFA at 4°C for 1 h. Then, tissues were washed in PBS, dehydrated in 30% sucrose overnight at 4°C and embedded in OCT (Sakura). For staining, cryosections (8-10 µm) were washed in PBS, incubated in blocking buffer [5% normal donkey serum (Jackson ImmunoResearch), 0.1% Triton X-100 in PBS] for 30 min at room temperature then stained with the primary antibodies overnight at 4°C. Signals were developed with Alexa fluorophore-conjugated or horseradish peroxidase-conjugated secondary antibodies: Alexa 488 donkey anti-rabbit (Invitrogen, A21206), Alexa 555 donkey anti-rabbit (Invitrogen, A31572), Alexa 647 donkey anti-rabbit (Invitrogen, A31573), Alexa 488 donkey anti-goat (Invitrogen, A11055), Alexa 555 donkey anti-goat (Invitrogen, A21432), Dylight 549 donkey anti-rat IgG(H + L) (Jackson ImmunoResearch, 712-505-153), Alexa 488 donkey anti-rat (Invitrogen, A21808), immPRESS-rat immunoglobulin (goat) (Vector Laboratories, MP-7444-15), immPRESS-goat immunoglobulin (horse) (Vector Laboratories, MP-7405-50), immPRESS-rabbit immunoglobulin (horse) (Vector Laboratories, MP-7401-50). The tyramide signal amplification kit (PerkinElmer) was used to amplify weak signals. Nuclei were counterstained with 4′6-diamidino-2-phenylindole (DAPI, Vector Laboratories). The following antibodies were used: tdTomato (Rockland, 600-401-379, 1:500), tdTomato (ChromoTek, 5F8, 1:100), GFP (Invitrogen, A11122, 1:500), GFP (Abcam, ab6662, 1:500), GFP (Nacalai Tesque, 04404-84, 1:500), PDGFRa (R&D Systems, AF1062, 1:500), VE-cadherin (R&D Systems, AF1002, 1:100), CD45 (eBioscience, 25-0451, 1:400), Troponin I (Abcam, ab56357, 1:200), E-cadherin (Cell Signaling, 3195, 1:100), cytokeratin 19 (CK19, Developmental Studies Hybridoma Bank, TROMA-III, 1:100), HNF4a (Cell Signaling, 3113s, 1:1000), Ki67 (Thermo Scientific, RM-9106-S0, 1:200), GS (Abcam, ab49873, 1:1000), p21 (Abcam, ab188224, 1:500). Immunostaining images were acquired using a Zeiss confocal microscope (LSM710) or a Nikon A1 confocal microscope.

Proliferation detection

Mice received an intraperitoneal injection of 10 mg kg^{-1} EdU (Invitrogen, A10044) at the indicated time. To detect the proliferation of fibroblasts in the heart, mice were sacrificed 24 h after the EdU injection. Cryosections were obtained and incubated with primary and secondary antibodies as described above, and EdU signal was developed using the Click-iT EdU Alexa Fluor 647 Imaging Kit (Life Technologies, C10340) following the manufacturer's instructions. Images were acquired using a Zeiss confocal microscope (LSM710) or a Nikon A1 confocal microscope.

Sirius Red staining

Sirius Red staining was designed to assess fibrotic tissue formation after injury and was performed as described previously (Liu et al., 2019). Cryosections were fixed in 4% PFA for 15 min and washed in PBS for 15 min, then fixed overnight in Bouins' solution (5% acetic acid, 9% formaldehyde, 0.9% picric acid). Afterwards, sections were stained with 0.1% Fast Green (Fisher Scientific) for 3 min and incubated in 1% acetic acid for 1 min followed by incubation with 0.1% Sirius Red (Sigma-Aldrich) for 2 min. Sections were rinsed with tap water before incubation into the staining solution. Finally, slides were dehydrated in 100% ethanol twice, cleared in xylene, and mounted with resinous medium. Images were obtained on an Olympus microscope (BX53).

Injury models

MI was performed in mice as described previously (Li et al., 2018). In detail, mice were anaesthetized with isoflurane and their chest hair was shaved. Mice were ventilated and anaesthetized by tracheal intubation, which was connected to an isoflurane gas machine and respiratory machine (Harvard Apparatus). An incision of ∼1 cm was made between the third and fourth ribs to expose heart. Then the left anterior descending coronary artery was ligated with a suture in the upper third region. The incision was then closed after surgery. The mice were supplied with oxygen for a few minutes until the mice woke up, and they were kept in a warm environment until they displayed normal behavior.

Development (2020) 147, dev183830. doi:10.1242/dev.183830

MI-reperfusion injury was performed as described previously (He et al., 2017). In brief, mice were anaesthetized as described for MI injury. Afterwards, the chest skin was disinfected and an incision was made to expose heart. Then, the left anterior descending coronary artery was ligated with a suture and a hose was inserted in between the suture and the ligated site for 30 min. After ligation, the left anterior descending coronary artery was re-perfused by removing the suture and hose. The incision was then closed after surgery. The mice were supplied with oxygen until the mice woke up, and they were kept warm until they recovered normal behavior.

For the CCl_4-induced acute injury, mice were intraperitoneally injected with a single dose of 1 µl/g body weight CCl_4, with the CCl_4 being dissolved at 1:3 in corn oil.

For the DDC diet, mice were fed with standard mouse diet (Harlan Teklad, 5015) containing 0.1% DDC (Sigma-Aldrich).

Hepatocyte isolation

For p21 overexpression detection, we isolated hepatocytes from the liver of *Alb-CreER;R26-p21-GFP* mice treated with tamoxifen or oil. Hepatocytes were isolated by standard two-step collagenase perfusion as described previously (Pu et al., 2016). Briefly, mice were anaesthetized and an incision was made in the lower abdomen to expose the liver with inferior vena cava and portal vein when the mouse was no longer responsive. A cannula was inserted into the inferior vena cava and secured with a suture around the cannula. The portal vein was cut and the mouse liver was perfused with perfusion medium for 10-15 min. The liver was next perfused with medium containing collagenase type I (Invitrogen) for 10 min. After adequate digestion, the liver was dissected in a Petri dish and passed through a 70 mm filter followed by centrifugation for 2 min at 50 ***g***. Non-hepatocytes cells remained in the supernatant, which was discarded, and the hepatocytes pellet was re-suspended in DMEM medium. The above washing step was repeated three times to remove non-hepatocytes. Washed cells were further purified by Percoll. Viable cells remaining at the bottom of the Percoll were washed and collected.

RNA isolation and quantitative RT-PCR

Total RNA was extracted from hepatocytes isolated from *Alb-CreER;R26-p21-GFP* mice treated with tamoxifen or oil. Hepatocytes were lysed with Trizol, and total RNA was extracted according to the manufacturer's instructions (Invitrogen). Then, RNA was reverse transcribed into cDNA using a Prime Script RT kit (Takara). The SYBR Green qPCR master mix (Applied Biosystems) was used and quantitative RT-PCR was performed on a StepOnePlus Real-Time PCR System (Applied Biosystems). *Gapdh* was used as internal control. The primers for *p21* and *Gapdh* RT-PCR are listed below: *Gapdh* 5′-TTGTCTCCTGCGACTTCAAC-3′ (forward), 5′-GTC-ATACCAGGAAATGAGCTTG-3′ (reverse); *p21* 5′-GGAACATCTCAG-GGCCGAAA-3′ (forward), 5′-CAATCTGCGCTTGGAGTGAT-3′ (reverse).

AAV8-TBG-Dre virus production and injection

AAV8-TBG-Dre virus was generated by Taitool Bioscience, Shanghai. Mice at the age of 8 weeks were induced with AAV8-TBG-Dre virus or AAV8-TBG-null virus (AAV8-control). The virus was diluted in PBS. Virus was administered by tail vein injection at a dose of 3×10^{11} once a week for 2 weeks. The tail vein injection volume was limited to 200 µl. Mice were given a 2-week washout period before being placed on a DDC diet.

Genomic PCR

Genomic DNA was extracted from the mouse tail. Tissues were lysed with Proteinase K overnight at 55°C, followed by centrifugation at maximum speed (21,000 ***g***) for 8 min to acquire supernatant with genomic DNA. DNA was deposited by adding isopropanol, and washing in 70% ethanol. All mice were genotyped with specific PCR primers. See Table S1 for a list of genomic PCR primers.

Echocardiography

To determine ejection fraction (EF) as well as fraction shortening (FS), echocardiography was performed on mice at 1 week before MI and 1 week, 4 weeks and 8 weeks after MI, using a digital ultrasound system (Vevo2100 Imaging System, Visual Sonics). The mice were measured under isoflurane anesthesia. All parameters were analyzed using original parameters and accompanying software.

Statistics

Tissue samples were randomized and blinded for analyzers. Data are presented as mean±s.e.m. Statistical analysis was performed by two-tailed unpaired Student's *t*-test for comparison of differences between two groups. $P<0.05$ was considered to be statistically significant.

Acknowledgements

We thank Dr Guoqiang Gu for sharing *CK19-CreER*, and Shanghai Biomodel Organism Co., Ltd. for mouse generation.

Competing interests

The authors declare no competing or financial interests.

Author contributions

Methodology: J.W., R.S., J.F.; Formal analysis: B.Z.; Data curation: W.P., X. Han, L.H., Y.L., X. Huang, M.Z., Z.L., W.Y.; Writing - original draft: W.P., B.Z.; Writing - review & editing: Q.-D.W., D.C., Y.J., Y.N., B.Z.; Project administration: W.P., B.Z.; Funding acquisition: B.Z.

Funding

This work was supported by the Strategic Priority Research Program of the Chinese Academy of Sciences (CAS; XDB19000000, XDA16010507), National Key Research and Development Program of China (2018YFA0107900, 2018YFA0108100, 2016YFC1300600, 2017YFC1001303, 2017YFA0505500), National Natural Science Foundation of China (31730112, 91639302, 31625019, 81761138040, 9184920003, 31571503, 31501172, 31601168, 31701292, 91749122, 81872241, 81872132, 31801215), the Pearl River Talent Recruitment Program of Guangdong Province (2017ZT07S347), Key Project of Frontier Sciences of CAS (QYZDB-SSW-SMC003), Shanghai Science and Technology Commission (17ZR1449600, 17ZR1449800), Shanghai Yangfan Project (16YF1413400, 18YF1427600) and Shanghai Rising-Star Program (15QA1404300), China Postdoctoral Innovative Talent Support Program and China Young Talents Lift Engineering, AstraZeneca, Boehringer Ingelheim, a Sanofi-SIBS Fellowship, and a Royal Society Newton Advanced Fellowship.

Supplementary information

Supplementary information available online at http://dev.biologists.org/lookup/doi/10.1242/dev.183830.supplemental

Peer review history

The peer review history is available online at https://dev.biologists.org/lookup/doi/10.1242/dev.183830.reviewer-comments.pdf

References

Anastassiadis, K., Fu, J., Patsch, C., Hu, S., Weidlich, S., Duerschke, K., Buchholz, F., Edenhofer, F. and Stewart, A. F. (2009). Dre recombinase, like Cre, is a highly efficient site-specific recombinase in E. coli, mammalian cells and mice. *Dis. Model. Mech.* **2**, 508-515. doi:10.1242/dmm.003087

Augustin, H. G. and Koh, G. Y. (2017). Organotypic vasculature: from descriptive heterogeneity to functional pathophysiology. *Science* **357**, eaal2379. doi:10.1126/science.aal2379

Barker, N., van Es, J. H., Kuipers, J., Kujala, P., van den Born, M., Cozijnsen, M., Haegebarth, A., Korving, J., Begthel, H., Peters, P. J. et al. (2007). Identification of stem cells in small intestine and colon by marker gene Lgr5. *Nature* **449**, 1003-1007. doi:10.1038/nature06196

Bergmann, O., Bhardwaj, R. D., Bernard, S., Zdunek, S., Barnabé-Heider, F., Walsh, S., Zupicich, J., Alkass, K., Buchholz, B. A., Druid, H. et al. (2009). Evidence for cardiomyocyte renewal in humans. *Science* **324**, 98-102. doi:10.1126/science.1164680

Buckingham, M., Meilhac, S. and Zaffran, S. (2005). Building the mammalian heart from two sources of myocardial cells. *Nat. Rev. Genet.* **6**, 826-835. doi:10.1038/nrg1710

Carlson, M. E., Hsu, M. and Conboy, I. M. (2008). Imbalance between pSmad3 and Notch induces CDK inhibitors in old muscle stem cells. *Nature* **454**, 528-532. doi:10.1038/nature07034

Choi, T. Y., Ninov, N., Stainier, D. Y. R. and Shin, D. (2014). Extensive conversion of hepatic biliary epithelial cells to hepatocytes after near total loss of hepatocytes in zebrafish. *Gastroenterology* **146**, 776-788. doi:10.1053/j.gastro.2013.10.019

Chu, A. S., Diaz, R., Hui, J.-J., Yanger, K., Zong, Y., Alpini, G., Stanger, B. Z. and Wells, R. G. (2011). Lineage tracing demonstrates no evidence of cholangiocyte

epithelial-to-mesenchymal transition in murine models of hepatic fibrosis. *Hepatology* **53**, 1685-1695. doi:10.1002/hep.24206

Deng, X., Zhang, X., Li, W., Feng, R.-X., Li, L., Yi, G.-R., Zhang, X.-N., Yin, C., Yu, H.-Y., Zhang, J.-P. et al. (2018). Chronic liver injury induces conversion of biliary epithelial cells into hepatocytes. *Cell Stem Cell* **23**, 114-122.e3. doi:10.1016/j.stem.2018.05.022

Español-Suñer, R., Carpentier, R., Van Hul, N., Legry, V., Achouri, Y., Cordi, S., Jacquemin, P., Lemaigre, F. and Leclercq, I. A. (2012). Liver progenitor cells yield functional hepatocytes in response to chronic liver injury in mice. *Gastroenterology* **143**, 1564-1575.e7. doi:10.1053/j.gastro.2012.08.024

Font-Burgada, J., Shalapour, S., Ramaswamy, S., Hsueh, B., Rossell, D., Umemura, A., Taniguchi, K., Nakagawa, H., Valasek, M. A., Ye, L. et al. (2015). Hybrid periportal hepatocytes regenerate the injured liver without giving rise to cancer. *Cell* **162**, 766-779. doi:10.1016/j.cell.2015.07.026

He, J., Lu, H., Zou, Q. and Luo, L. (2014). Regeneration of liver after extreme hepatocyte loss occurs mainly via biliary transdifferentiation in zebrafish. *Gastroenterology* **146**, 789-800.e8. doi:10.1053/j.gastro.2013.11.045

He, L., Huang, X., Kanisicak, O., Li, Y., Wang, Y., Li, Y., Pu, W., Liu, Q., Zhang, H., Tian, X. et al. (2017a). Preexisting endothelial cells mediate cardiac neovascularization after injury. *J. Clin. Invest.* **127**, 2968-2981. doi:10.1172/JCI93868

He, L., Li, Y., Li, Y., Pu, W., Huang, X., Tian, X., Wang, Y., Zhang, H., Liu, Q., Zhang, L. et al. (2017b). Enhancing the precision of genetic lineage tracing using dual recombinases. *Nat. Med.* **23**, 1488-1498. doi:10.1038/nm.4437

Heallen, T., Zhang, M., Wang, J., Bonilla-Claudio, M., Klysik, E., Johnson, R. L. and Martin, J. F. (2011). Hippo pathway inhibits Wnt signaling to restrain cardiomyocyte proliferation and heart size. *Science* **332**, 458-461. doi:10.1126/science.1199010

Hermann, M., Stillhard, P., Wildner, H., Seruggia, D., Kapp, V., Sánchez-Iranzo, H., Mercader, N., Montoliu, L., Zeilhofer, H. U. and Pelczar, P. (2014). Binary recombinase systems for high-resolution conditional mutagenesis. *Nucleic Acids Res.* **42**, 3894-3907. doi:10.1093/nar/gkt1361

Hogan, B. L. M., Barkauskas, C. E., Chapman, H. A., Epstein, J. A., Jain, R., Hsia, C. C. W., Niklason, L., Calle, E., Le, A., Randell, S. H. et al. (2014). Repair and regeneration of the respiratory system: complexity, plasticity, and mechanisms of lung stem cell function. *Cell Stem Cell* **15**, 123-138. doi:10.1016/j.stem.2014.07.012

Kanisicak, O., Khalil, H., Ivey, M. J., Karch, J., Maliken, B. D., Correll, R. N., Brody, M. J. J., Lin, S.-C., Aronow, B. J., Tallquist, M. D. et al. (2016). Genetic lineage tracing defines myofibroblast origin and function in the injured heart. *Nat. Commun.* **7**, 12260. doi:10.1038/ncomms12260

Kaur, H., Takefuji, M., Ngai, C. Y., Carvalho, J., Bayer, J., Wietelmann, A., Poetsch, A., Hoelper, S., Conway, S. J., Möllmann, H. et al. (2016). Targeted ablation of periostin-expressing activated fibroblasts prevents adverse cardiac remodeling in mice. *Circ. Res.* **118**, 1906-1917. doi:10.1161/CIRCRESAHA.116.308643

Kim, C. F. B., Jackson, E. L., Woolfenden, A. E., Lawrence, S., Babar, I., Vogel, S., Crowley, D., Bronson, R. T. and Jacks, T. (2005). Identification of bronchioalveolar stem cells in normal lung and lung cancer. *Cell* **121**, 823-835. doi:10.1016/j.cell.2005.03.032

Li, Y., He, L., Huang, X., Bhaloo, S. I., Zhao, H., Zhang, S., Pu, W., Tian, X., Li, Y., Liu, Q. et al. (2018). Genetic lineage tracing of nonmyocyte population by dual recombinases. *Circulation* **138**, 793-805. doi:10.1161/CIRCULATIONAHA.118.034250

Lin, Z., von Gise, A., Zhou, P., Gu, F., Ma, Q., Jiang, J., Yau, A. L., Buck, J. N., Gouin, K. A., van Gorp, P. R. R. et al. (2014). Cardiac-specific YAP activation improves cardiac function and survival in an experimental murine MI model. *Circ. Res.* **115**, 354-363. doi:10.1161/CIRCRESAHA.115.303632

Liu, Q., Liu, K., Cui, G., Huang, X., Yao, S., Guo, W., Qin, Z., Li, Y., Yang, R., Pu, W. et al. (2019). Lung regeneration by multipotent stem cells residing at the bronchioalveolar-duct junction. *Nat. Genet.* **51**, 728-738. doi:10.1038/s41588-019-0346-6

Madisen, L., Zwingman, T. A., Sunkin, S. M., Oh, S. W., Zariwala, H. A., Gu, H., Ng, L. L., Palmiter, R. D., Hawrylycz, M. J., Jones, A. R. et al. (2010). A robust and high-throughput Cre reporting and characterization system for the whole mouse brain. *Nat. Neurosci.* **13**, 133-140. doi:10.1038/nn.2467

Malato, Y., Naqvi, S., Schürmann, N., Ng, R., Wang, B., Zape, J., Kay, M. A., Grimm, D. and Willenbring, H. (2011). Fate tracing of mature hepatocytes in mouse liver homeostasis and regeneration. *J. Clin. Invest.* **121**, 4850-4860. doi:10.1172/JCI59261

Marshall, A., Rushbrook, S., Davies, S. E., Morris, L. S., Scott, I. S., Vowler, S. L., Coleman, N. and Alexander, G. (2005). Relation between hepatocyte G1 arrest, impaired hepatic regeneration, and fibrosis in chronic hepatitis C virus infection. *Gastroenterology* **128**, 33-42. doi:10.1053/j.gastro.2004.09.076

Mohamed, T. M. A., Ang, Y.-S., Radzinsky, E., Zhou, P., Huang, Y., Elfenbein, A., Foley, A., Magnitsky, S. and Srivastava, D. (2018). Regulation of cell cycle to stimulate adult cardiomyocyte proliferation and cardiac regeneration. *Cell* **173**, 104-116.e12. doi:10.1016/j.cell.2018.02.014

Moore-Morris, T., Guimarães-Camboa, N., Banerjee, I., Zambon, A. C., Kisseleva, T., Velayoudon, A., Stallcup, W. B., Gu, Y., Dalton, N. D., Cedenilla, M. et al. (2014). Resident fibroblast lineages mediate pressure overload-induced cardiac fibrosis. *J. Clin. Invest.* **124**, 2921-2934. doi:10.1172/JCI74783

Porrello, E. R., Mahmoud, A. I., Simpson, E., Hill, J. A., Richardson, J. A., Olson, E. N. and Sadek, H. A. (2011). Transient regenerative potential of the neonatal mouse heart. *Science* **331**, 1078-1080. doi:10.1126/science.1200708

Pu, W., Zhang, H., Huang, X., Tian, X., He, L., Wang, Y., Zhang, L., Liu, Q., Li, Y., Li, Y. et al. (2016). Mfsd2a+ hepatocytes repopulate the liver during injury and regeneration. *Nat. Commun.* **7**, 13369. doi:10.1038/ncomms13369

Pu, W., He, L., Han, X., Tian, X., Li, Y., Zhang, H., Liu, Q., Huang, X., Zhang, L., Wang, Q.-D. et al. (2018). Genetic targeting of organ-specific blood vessels. *Circ. Res.* **123**, 86-99. doi:10.1161/CIRCRESAHA.118.312981

Raven, A., Lu, W.-Y., Man, T. Y., Ferreira-Gonzalez, S., O'Duibhir, E., Dwyer, B. J., Thomson, J. P., Meehan, R. R., Bogorad, R., Koteliansky, V. et al. (2017). Cholangiocytes act as facultative liver stem cells during impaired hepatocyte regeneration. *Nature* **547**, 350-354. doi:10.1038/nature23015

Red-Horse, K., Ueno, H., Weissman, I. L. and Krasnow, M. A. (2010). Coronary arteries form by developmental reprogramming of venous cells. *Nature* **464**, 549-553. doi:10.1038/nature08873

Richardson, M. M., Jonsson, J. R., Powell, E. E., Brunt, E. M., Neuschwander-Tetri, B. A., Bhathal, P. S., Dixon, J. B., Weltman, M. D., Tilg, H., Moschen, A. R. et al. (2007). Progressive fibrosis in nonalcoholic steatohepatitis: association with altered regeneration and a ductular reaction. *Gastroenterology* **133**, 80-90. doi:10.1053/j.gastro.2007.05.012

Rodrigo-Torres, D., Affò, S., Coll, M., Morales-Ibanez, O., Millán, C., Blaya, D., Alvarez-Guaita, A., Rentero, C., Lozano, J. J., Maestro, M. A. et al. (2014). The biliary epithelium gives rise to liver progenitor cells. *Hepatology* **60**, 1367-1377. doi:10.1002/hep.27078

Schaub, J. R., Malato, Y., Gormond, C. and Willenbring, H. (2014). Evidence against a stem cell origin of new hepatocytes in a common mouse model of chronic liver injury. *Cell Rep* **8**, 933-939. doi:10.1016/j.celrep.2014.07.003

Segal, J. M., Kent, D., Wesche, D. J., Ng, S. S., Serra, M., Oulès, B., Kar, G., Emerton, G., Blackford, S. J. I., Darmanis, S. et al. (2019). Single cell analysis of human foetal liver captures the transcriptional profile of hepatobiliary hybrid progenitors. *Nat. Commun.* **10**, 3350. doi:10.1038/s41467-019-11266-x

Simons, B. D. and Clevers, H. (2011). Strategies for homeostatic stem cell self-renewal in adult tissues. *Cell* **145**, 851-862. doi:10.1016/j.cell.2011.05.033

Tarlow, B. D., Pelz, C., Naugler, W. E., Wakefield, L., Wilson, E. M., Finegold, M. J. and Grompe, M. (2014). Bipotential adult liver progenitors are derived from chronically injured mature hepatocytes. *Cell Stem Cell* **15**, 605-618. doi:10.1016/j.stem.2014.09.008

Tian, X., Hu, T., Zhang, H., He, L., Huang, X., Liu, Q., Yu, W., He, L., Yang, Z., Zhang, Z. et al. (2013). Subepicardial endothelial cells invade the embryonic ventricle wall to form coronary arteries. *Cell Res.* **23**, 1075-1090. doi:10.1038/cr.2013.83

Tzahor, E. and Poss, K. D. (2017). Cardiac regeneration strategies: staying young at heart. *Science* **356**, 1035-1039. doi:10.1126/science.aam5894

Ubil, E., Duan, J., Pillai, I. C. L., Rosa-Garrido, M., Wu, Y., Bargiacchi, F., Lu, Y., Stanbouly, S., Huang, J., Rojas, M. et al. (2014). Mesenchymal-endothelial transition contributes to cardiac neovascularization. *Nature* **514**, 585-590. doi:10.1038/nature13839

Yanger, K., Knigin, D., Zong, Y., Maggs, L., Gu, G., Akiyama, H., Pikarsky, E. and Stanger, B. Z. (2014). Adult hepatocytes are generated by self-duplication rather than stem cell differentiation. *Cell Stem Cell* **15**, 340-349. doi:10.1016/j.stem.2014.06.003

Zeisberg, M., Hanai, J., Sugimoto, H., Mammoto, T., Charytan, D., Strutz, F. and Kalluri, R. (2003). BMP-7 counteracts TGF-β1-induced epithelial-to-mesenchymal transition and reverses chronic renal injury. *Nat. Med.* **9**, 964-968. doi:10.1038/nm888

Zhang, H., Pu, W., Li, G., Huang, X., He, L., Tian, X., Liu, Q., Zhang, L., Wu, S. M., Sucov, H. M. et al. (2016). Endocardium minimally contributes to coronary endothelium in the embryonic ventricular free walls. *Circ. Res.* **118**, 1880-1893. doi:10.1161/CIRCRESAHA.116.308749

Zhou, B., Honor, L. B., He, H., Ma, Q., Oh, J.-H., Butterfield, C., Lin, R.-Z., Melero-Martin, J. M., Dolmatova, E., Duffy, H. S. et al. (2011). Adult mouse epicardium modulates myocardial injury by secreting paracrine factors. *J. Clin. Invest.* **121**, 1894-1904. doi:10.1172/JCI45529